

Quantitative Measurements of the Temperature-Dependent Microscopic and Macroscopic Dynamics of a Molecular Dopant in a Conjugated Polymer

Jun Li,[†] Correy Koshnick,[‡] Souleymane O. Diallo,^{||} Sophia Ackling,[#] David M. Huang,[#] Ian E. Jacobs,[‡] Thomas Harrelson,[†] Kunlun Hong,[⊥] Guangwu Zhang,[§] Joseph Beckett,[§] Mark Mascal,[§] and Adam J. Moulé^{*,†}

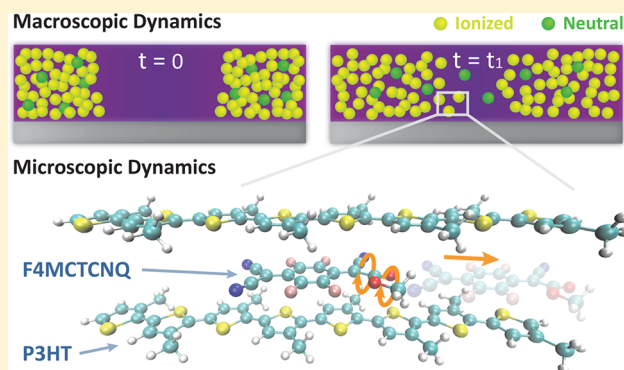
[†]Department of Chemical Engineering, [‡]Department of Materials Science and Engineering, and [§]Department of Chemistry, University of California, Davis, Davis, California 95616, United States

^{||}Neutron Scattering Science Division and [⊥]Center for Nanophase Materials Sciences, Oak Ridge National Laboratory, Oak Ridge, Tennessee 37831, United States

[#]Department of Chemistry, School of Physical Sciences, The University of Adelaide, Adelaide, SA 5005, Australia

S Supporting Information

ABSTRACT: Understanding the nature of dopant dynamics in the solid state is critical for improving the longevity and stability of organic electronic devices and for optimizing the doping-induced solubility control (DISC) patterning method. In this work, we use quasi-elastic neutron scattering (QENS) and fluorescence quenching techniques to develop a comprehensive picture of both the microscopic and macroscopic dynamics of the soluble p-type molecular dopant tetrafluoromethyloxycarbonyltricyanoquinodimethane (F4MCTCNQ) in the conductive polymer poly(3-hexylthiophene-2,5-diyl) (P3HT). Specifically, fast dynamics (ps–ns) of the dopant, such as the methyl and the methoxycarbonyl group rotations, are observed in QENS experiments. From confocal fluorescence microscope experiments, longer-range/slower dopant diffusion (ms–days) is captured. However, in order to fit these data, it is necessary to incorporate a Langmuir isotherm equilibrium between the neutral and ionized dopant molecules. Ionized F4MCTCNQ is strongly favored by the equilibrium, but it diffuses 3 orders of magnitude slower than neutral species. Moreover, the macroscopic diffusion is found to depend mostly on the minority concentration of neutral dopant molecules in the film. Finally, the global diffusion coefficient of the monoester-substituted dopant F4MCTCNQ is shown to be more than 1 order of magnitude smaller than that of the widely used dopant F4TCNQ.



INTRODUCTION

The successful development of organic electronic devices, such as organic photovoltaics (OPVs),^{1,2} organic light-emitting diodes (OLEDs),^{3,4} and organic field-effect transistors (OFETs),^{5,6} is largely attributable to the tunability of their electrical properties. Like inorganic semiconductors, organic semiconductors (OSCs) can be doped to facilitate increased charge transport^{7,8} as well as decreased injection or extraction barriers via changes in the Fermi energy.⁹ However, the undesired diffusion of dopants in organic electronic architectures has been known to cause serious stability and longevity issues.^{10–12} Controlling dopant diffusion is also an important aspect of doping-induced solubility control (DISC), a new patterning method recently developed which allows the solubility of a conductive polymer to be switched on and off by doping and dedoping, respectively.^{13–15} It has also been demonstrated that DISC is capable of using both vapor and

solution processes to achieve micrometer and submicrometer resolution, respectively, in a method that is compatible with roll-to-roll solution processing.^{13,16} For DISC patterning, the lateral diffusion of the dopant limits the ultimate resolution of the pattern. Therefore, for both the stability of completed organic devices and for fabrication of these devices using solution compatible methods, understanding the dynamics of the dopants is extremely important to further application development.

The measurement of small molecular dopant diffusion is particularly challenging because dopants are present in trace quantities and composed of the same light elements (C, H, O, N, S) as the host OSCs. Most of these studies so far have

Received: March 30, 2017

Revised: May 31, 2017

62 focused on the diffusion of dopants from one layer to another
 63 in a vertical layer stack. These samples are prepared by either
 64 vacuum evaporating or laminating doped and undoped layers of
 65 materials. Secondary ion mass spectrometry (SIMS) is by far
 66 the most commonly used technique for diffusion studies due to
 67 its high spatial and depth resolution in differentiating
 68 molecules. A recent study shows that SIMS can be utilized to
 69 monitor the diffusion of 2,3,5,6-tetrafluoro-7,7,8,8-tetracyano-
 70 quinodimethane (F4TCNQ), which is a widely used p-type
 71 molecular dopant, in the hole transport layer of OLEDs.¹⁷ The
 72 SIMS signal from the fluorine atoms gives a unique isotopic
 73 label. Similar work using SIMS was also performed more
 74 recently on the diffusion of the soluble p-dopant molybdenum
 75 tris[1-(methoxycarbonyl)-2-(trifluoromethyl)-ethane-1,2-di-
 76 thiolene] (Mo(tfd-CO₂Me)₃) into polymer and polymer blend
 77 films using the Mo label.¹⁸ Likewise, excellent work was
 78 conducted by Treat et al. where the diffusion of phenyl-C₆₁-
 79 butyric acid methyl ester (PCBM) in poly(3-hexylthiophene-
 80 2,5-diyl) (P3HT) was quantified using SIMS and a deuterium-
 81 labeled PCBM (*d*-PCBM).¹⁹ The same group also quantified
 82 the lateral diffusion of *d*-PCBM in P3HT using dynamic SIMS,
 83 yielding a one-dimensional diffusion coefficient using Fick's
 84 second law.²⁰ However, SIMS is a destructive technique, and
 85 additional etching steps are needed. In addition, a unique atom
 86 or isotopic labeling is required in order to use SIMS. Other
 87 measurement techniques, such as X-ray photoelectron spec-
 88 troscopy (XPS), ultraviolet photoelectron spectroscopy (UPS),
 89 neutron/X-ray/visible light scattering, and photoluminescence,
 90 have also been used to measure the diffusion of dopants in
 91 layered samples.^{21–29} Most of these studies reported whether
 92 dopants diffused beyond their original layer and at which
 93 temperature threshold. Although some were able to quantify
 94 dopant concentration at an interface or surface, only one study
 95 was able to measure diffusion as a function of distance and time.
 96 Thus, Fischer et al. quantified the temperature dependence of
 97 the diffusion coefficient in a vertical geometry using a time-
 98 resolved optical technique.²⁴ Finally, a series of articles have
 99 reported the observation of dopant diffusion (or lack thereof)
 100 by creating bi- or trilayers and subsequently measuring changes
 101 in the electronic properties of layer stack.^{30–34} For these
 102 electronic measurements, the movement of dopants is inferred
 103 but cannot be quantified.

104 Previous studies have shown that dopant molecules can
 105 diffuse in a small molecule or polymer OSC host. It is known
 106 that larger dopant molecules diffuse more slowly but also have
 107 been shown to disturb the packing of the OSC and thereby to
 108 increase disorder in the local density of states.³⁵ Very few
 109 studies have quantified the diffusion rate of dopants. It has been
 110 assumed that the onset of diffusion occurs as a result of heating
 111 to above the glass transition temperature (*T*_g) of host OSC.
 112 However, one study showed that F4TCNQ diffuses at room
 113 temperature in P3HT²³ and another showed that PCBM
 114 diffuses into P3HT at 50 °C, which is below the *T*_g of P3HT.¹⁹
 115 To the best of our knowledge, no molecular level studies have
 116 looked into the mechanism for dopant binding or investigated
 117 how the properties of the host material affect the onset of
 118 dopant diffusion.

119 In this article, we investigate the temperature-dependent
 120 microscopic and macroscopic dynamics of the soluble p-type
 121 molecular dopant tetrafluoromethyloxycarbonyltricyano-
 122 quinodimethane (F4MCTCNQ) in P3HT. F4MCTCNQ is
 123 chosen due to its superior solubility/miscibility and thereby
 124 increased doping efficiency compared with F4TCNQ.³⁶ The

chemical structures of the materials investigated in this paper
 are shown in Figure 1. F4MCTCNQ was also chosen because

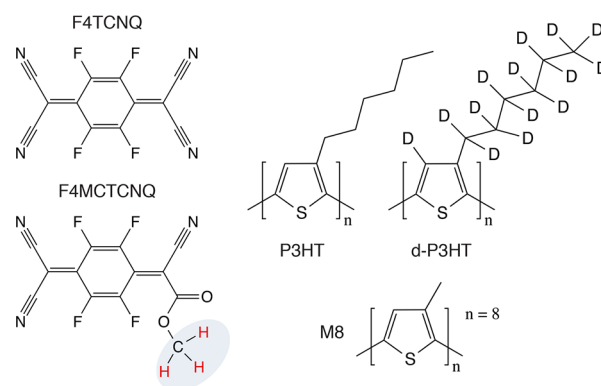


Figure 1. Chemical structures of F4TCNQ, F4MCTCNQ, P3HT, *d*-P3HT, and the simplified P3HT analogue (M8) investigated in this work.

its methyl group carries three identical protons that can be used
 as a unique isotopic label in neutron scattering experiments.
 Quasi-elastic neutron scattering (QENS) is a well-established
 nondestructive technique to probe dynamic processes in soft
 matter.³⁷ In the first part of this article, we use QENS to
 measure the dynamics of F4MCTCNQ at the molecular scale
 in a sample of fully deuterated P3HT (*d*-P3HT). The protons
 on the F4MCTCNQ are the only hydrogen sites in the system,
 and ¹H has a much larger inelastic scattering cross section than
 any other isotope in the sample, allowing us to track the
 temperature-dependent motions of the dopant molecule only.
 The diffusion rate and jump distance for various microscopic
 motions are measured, and the motions are assigned with the
 aid of density functional theory (DFT) calculations. In the
 second part of the article, we use confocal fluorescence
 spectroscopy to spatially and temporally track the
 F4MCTCNQ concentration in patterned P3HT films, which
 allows us to quantify the macroscopic diffusion of the dopant.
 We show that macroscopic diffusion is principally dependent
 on the minority concentration of neutral dopant molecules in
 the film. This multiscale investigation gives an unprecedented
 mechanistic insight into dopant diffusion in OSCs.

EXPERIMENTAL SECTION

Materials. P3HT (regioregular >98%, *M*_n = 54–75 kDa), 150
 chlorobenzene, deuterated chlorobenzene, and molybdenum oxide
 (MoO₃) were purchased from Sigma-Aldrich. *d*-P3HT (regioregular
 >97%) and F4MCTCNQ were synthesized using the methods
 reported in the literature.^{36,38} All chemicals were used as received
 unless otherwise indicated. PELCO TEM grids (1GN400, nickel) were
 purchased from Ted Pella, Inc.

Sample Preparation and Measurements. Neutron Scattering.
 To prepare the blend sample for QENS measurements, solutions of
 F4MCTCNQ and *d*-P3HT in deuterated chlorobenzene were first
 mixed to achieve a 17% mole fraction of dopant to polymer. The blend
 solution was then drop-cast onto a clean glass slide. The sample was
 placed into a vacuum chamber to completely evaporate the solvent.
 The resulting blend layer was scraped from the glass slide using a clean
 razor blade. Both blend and neat samples were ground to a power
 using a mortar and pestle for 15 min and then weighed prior to being
 loaded into a 0.5 mm thick flat aluminum container for further
 analysis.

QENS measurements were performed on the backscattering
 spectrometer called BASIS at the Spallation Neutron Source (SNS)

170 at Oak Ridge National Laboratory (ORNL) with an energy resolution
171 of 3.5 μeV (full width at half-maximum, fwhm), a dynamic range of
172 $\pm 170 \mu\text{eV}$, and a scattering wavevector Q range from 0.3 to 2.0 \AA^{-1} .³⁹
173 The elastic scans were obtained from 50 to 375 K at a heating rate of 1
174 K/min, and the high statistical QENS spectra were recorded at 273,
175 323, and 373 K. The spectra collected at 50 K were used as the
176 instrument resolution function, and all the data were corrected for
177 detector efficiency using a vanadium standard.

178 **Confocal Spectroscopy.** To prepare samples for the macroscopic
179 diffusion measurements, P3HT films of ~ 50 nm thickness were first
180 obtained by spin-coating 10 mg/mL P3HT from a chlorobenzene
181 solution onto clean glass substrates (cleaned in ultrasonic baths of
182 acetone, 5% Mucosal detergent, and deionized water, followed by
183 drying with nitrogen and exposure to UV/ozone for 30 min). A TEM
184 grid (400 mesh; hole width 38 μm ; bar width 26 μm) was
185 subsequently placed onto the P3HT film using Kapton tape. Next, a
186 2.2 nm F4MCTCNQ layer was deposited onto the P3HT film using
187 an MBraun thermal evaporator at a deposition rate $\sim 0.1 \text{\AA}/\text{s}$ at ~ 80
188 $^\circ\text{C}$, followed by the deposition of 50 nm MoO_3 and 100 nm Ag, also
189 via evaporation. Prior to deposition, the evaporation chamber was
190 pumped down to a pressure of 5×10^{-6} mbar. Finally, the samples
191 were encapsulated in an epoxy resin under a glass coverslip to ensure
192 complete isolation from O_2 and H_2O . All fabrication steps were
193 performed inside a nitrogen glovebox.

194 The confocal fluorescence (FL) microscope images were obtained
195 on a Zeiss LSM 700 microscope equipped with a 488 nm laser and a
196 20 \times objective with 0.6 numerical aperture. These confocal FL images
197 (16-bit, 2048 \times 2048 pixels of 320 μm size) were captured at the same
198 position before and after annealing at various temperatures (298, 323,
199 348, and 373 K) for various time steps by tracking the position of the
200 marked center of the TEM grid.

201 **Data Analysis. Neutron Data Analysis.** For the data analysis, the
202 dynamic range was from -120 to $+120 \mu\text{eV}$. The relevant momentum
203 transfer range in this study was limited to 0.5–1.3 \AA^{-1} given the signal-
204 to-noise ratio, the flat-plate geometrical limit, and the uncertainty of
205 the background subtraction. DAVE software was used for data
206 reduction and analysis.⁴⁰ The neat *d*-P3HT spectra were subtracted
207 from the F4MCTCNQ doped *d*-P3HT spectra for all the QENS data
208 analyses to ensure that the signal from F4MCTCNQ could be isolated.
209 In general, the experimentally observed scattering intensity
210 $S_{\text{exp}}(Q, \omega)$ at each Q and temperature is expressed as the convolution
211 of the model function $S_{\text{model}}(Q, \omega)$ and the resolution function $R(Q, \omega)$,
212 plus a linear background term $B(Q, \omega)$:⁴¹

$$213 \quad S_{\text{exp}}(Q, \omega) = S_{\text{model}}(Q, \omega) \otimes R(Q, \omega) + B(Q, \omega) \quad (1)$$

214 Here, the model function can be separated into an elastic component
215 (a delta function $\delta(\omega)$) and a quasi-elastic contribution $S_{\text{qe}}(Q, \omega)$:

$$216 \quad S_{\text{model}}(Q, \omega) = \text{DWF}(Q)[A_0(Q)\delta(\omega) + (1 - A_0(Q))S_{\text{qe}}(Q, \omega)] \quad (2)$$

217 where $\text{DWF}(Q)$ is the Debye–Waller factor due to the vibrational
218 motions and $A_0(Q)$ is the elastic incoherent structure factor (EISF)
219 defined as the fraction of elastic scattering. The proposed expression
220 for $S_{\text{qe}}(Q, \omega)$ will be addressed in detail in the **Results and Discussion**
221 section.

222 **Macroscopic Diffusion Model.** The location of dopants within the
223 P3HT films was determined by measuring the fluorescence intensity of
224 P3HT as a function of position using a confocal microscope and 488
225 nm excitation. The concentration of the dopants was determined by
226 comparing to a calibration curve of fluorescence intensity in P3HT as a
227 function of known doping density and assuming that there is no
228 vertical doping gradient (reasonable for diffusion over μm in an ~ 50
229 nm thick film). A two-dimensional two-species (2D2S) diffusion
230 model was developed to fit the 2D doping profiles. The two diffusing
231 species in this model were treated using a Langmuir isotherm
232 equilibrium,⁴² which was preceded for P3HT/dopants in a previous
233 publication.¹⁴ In terms of detailed fits, the 2D concentration profile
234 images were initially evolved based on the above-mentioned diffusion
235 model and then evolved using a stepwise solution to Fick's second law.

The finite-difference method using a forward time-centered difference
236 scheme was used to evolve the model in time. After each profile was
237 evolved one time step into the future, the ratio of doped to undoped
238 F4MCTCNQ was re-equilibrated as a function of position and
239 concentration using the Langmuir equilibrium. In this rapid
240 equilibration, it is assumed that the reaction rate between two species
241 is much faster than the rate of diffusion. In doing so, the diffusion
242 coefficients for the two species could be treated as fitting parameters
243 and optimized based on minimization of the sum of squared residuals.
244

Computational Method. An eight-unit methyl-substituted oligo-
245 thiophene (M8) oligomer was used as a model for a P3HT chain. The
246 oligomer was optimized in isolation at the B3LYP/6-31G* level of
247 theory with Grimme D2 dispersion correction (B3LYP-D).^{43,44} In the
248 absence of a dielectric medium, two of these optimized oligomers were
249 then placed at two distinct intermolecular separations (6.30 and 6.96
250 \AA), and a F4MCTCNQ molecule was placed midway between and
251 parallel with the two M8 chains. These two intermolecular separations
252 were chosen based on the optimized M8/F4TCNQ system.⁴⁵ The
253 chains were fixed while the F4MCTCNQ was free to relax during a
254 geometry optimization at the B3LYP-D/6-31G* level. A dielectric
255 constant of 3.0 was used as it has been shown to be appropriate for
256 organic semiconductors.^{46–49} The lowest energy geometry was found
257 to be that with the ring of the F4MCTCNQ stacked over the central
258 inter-thiophene bond and the ester methyl group on the opposite side
259 of the M8 chain methyl groups. The two separations were chosen as
260 twice the distance between a single M8 chain and F4MCTCNQ
261 molecule from an unconstrained geometry optimization using B3LYP
262 with and without the dispersion correction, respectively. The two M8
263 oligomers were constrained in the optimization of the full system to
264 prevent unphysical wrapping of the chains around the F4MCTCNQ
265 molecule. These two intermolecular separations were used to give an
266 estimate of possible variations in the energy barriers to rotation and
267 translation due to variations in the interchain separation. Since it was
268 found that introducing solvent into this system does not affect the
269 intermolecular separation, the values from systems without the
270 dielectric continuum were used.
271

To calculate the potential energy barrier for F4MCTCNQ
272 translation along the polymer backbone axis, atoms in the M8 chains
273 were fixed while the F4MCTCNQ was free to relax in a set of
274 optimizations, subject to a position constraint applied by fixing one
275 atom in the F4MCTCNQ. This set of translation optimizations
276 spanned up to two thiophene units.
277

To calculate the potential energy barrier for F4MCTCNQ methyl
278 rotation between the two M8 chains for both interchain separations, all
279 atoms in the system excluding the ester methyl hydrogens were fixed,
280 and these hydrogens were free to relax in a set of optimizations subject
281 to dihedral angle constraints spanning 120 $^\circ$. In addition, calculations
282 on an isolated F4MCTCNQ molecule were performed, in which no
283 atom positions were fixed. Solvent was used in these calculations.
284 Similar calculations were performed to calculate the barrier for the
285 F4TCNQ methoxycarbonyl rotation, but only for the isolated
286 molecule and for the molecule between M8 chains separated by 6.96
287 \AA .
288

289 ■ RESULTS AND DISCUSSION

Part One: Microscopic Dynamics of Molecular
290 **Dopant. Elastic Incoherent Neutron Scattering.** The micro-
291 scopic dynamics of the F4MCTCNQ molecule were
292 investigated using neutron scattering. To determine the
293 temperature range at which the dynamic transitions of protons
294 take place and become observable on BASIS, facile elastic
295 incoherent neutron scattering experiments were performed
296 first. The elastic scans of the F4MCTCNQ doped *d*-P3HT
297 blend measured from 50 to 375 K at various Q values are
298 shown in **Figure 2a**. Generally, the elastic intensity decreases
299 monotonically with temperature due to Debye–Waller thermal
300 factors, while any observed dynamics of the species lead to
301 further reduction of the elastic intensity.⁵⁰ The divergence from 302

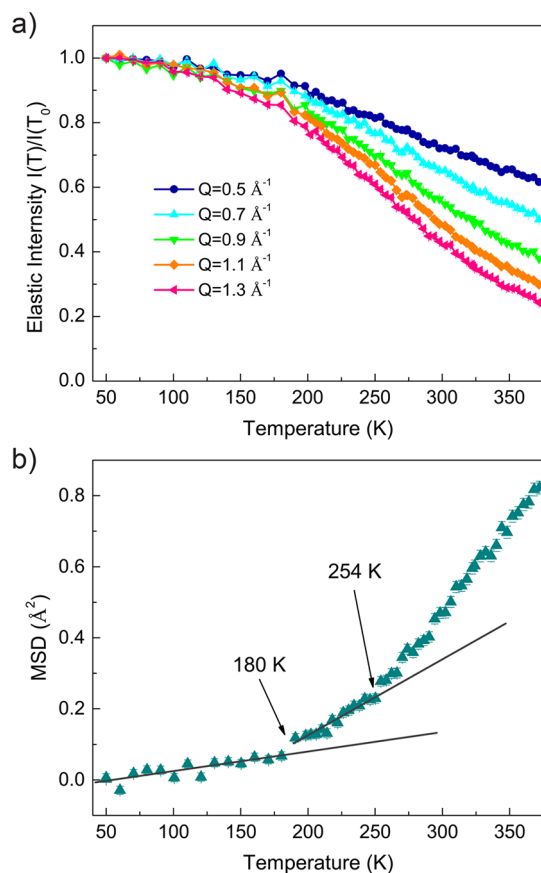


Figure 2. (a) Normalized elastic scattering intensity at various Q and (b) mean-square displacement (MSD) as a function of temperature for the F4MCTCNQ doped d -P3HT blend.

303 the monotonic decrease as a function of increasing temperature
304 indicates the onset of molecular motions for hydrogen sites in
305 this system.

306 To enhance conceptual understanding of this dynamic
307 process, the temperature dependence of the proton mean-
308 square displacement (MSD) determined from analysis of the
309 elastic scans (Supporting Information section 2) was
310 investigated. From Figure 2b, the MSD values do not vary
311 much at temperatures below 180 K because only some local
312 vibrations are expected to occur at such low temperatures. As
313 the temperature increases, two deviations (changes in slope)
314 are observed: one at about 180 K and another at 254 K. We
315 attribute the first deviation at ~ 180 K to the activation of
316 methyl group rotations, which are well-known to occur
317 between 100 and 220 K.^{51–53} On the other hand, the second
318 deviation at ~ 254 K implies that another dynamic transition
319 takes place in this temperature region. This transition could not
320 be assigned unambiguously without further analysis.

321 *Quasi-Elastic Neutron Scattering (QENS).* To assign the
322 dynamic transition starting at ~ 254 K, the high statistical
323 scattering data were collected at temperatures above 254 K in
324 order to capture this transition, and detailed analyses were
325 performed. As mentioned earlier, neat d -P3HT spectra were
326 also collected at the corresponding temperatures and subtracted
327 from the spectra of the doped samples (Supporting Information
328 section 3). In this manner, any changes of the scattering spectra
329 explicitly result from the dynamics of the hydrogen sites in the
330 dopants.

Representative neutron scattering spectra of subtracted
doped d -P3HT at $Q = 0.9 \text{ \AA}^{-1}$ at three temperatures (273, 323,
323, and 373 K) are shown in Figure 3. The experimental 333 333

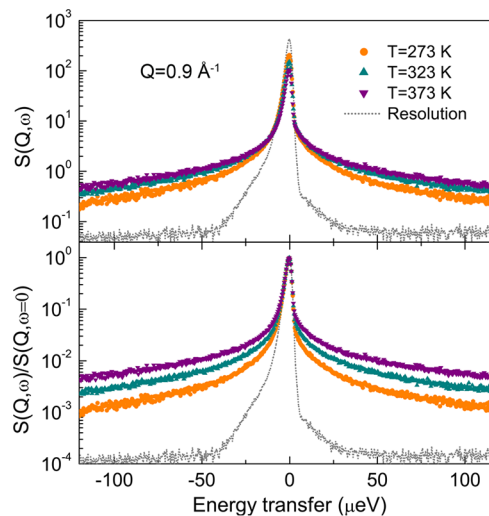


Figure 3. Representative BASIS spectra of subtracted doped d -P3HT at $Q = 0.9 \text{ \AA}^{-1}$ at 273 K (orange), 323 K (dark cyan), and 373 K (purple), along with the resolution function obtained at 50 K (gray dashed line). Both unnormalized (top) and normalized (bottom) data with respect to their intensity at $\hbar\omega = 0$ are shown.

334 resolution functions collected at 50 K are also plotted. In
335 general, the spectra can be described as a superposition of two
336 contributions: (1) a Gaussian distribution corresponding to the
337 elastic portion and (2) a broad shoulder in the quasi-elastic
338 region. The broadening of the quasi-elastic components with
339 increasing temperature seen from Figure 3 (it is more obvious
340 in their normalized spectra) provides clear evidence of the
341 occurrence of dynamic processes, which is consistent with the
342 MSD results from elastic scans. Similar broadening features are
343 also observed at other Q ranges (Supporting Information
344 Figures S2 and S3).

345 In order to extract diffusive information from QENS, the
346 experimental spectra were fit using a model function discussed
347 in the Data Analysis section (eqs 1 and 2). Again, since two
348 dynamic processes are observed above 254 K, two stretched
349 exponential relaxation (or Kohlrausch–Williams–Watts,
350 KWW) functions were included in the quasi-elastic term
351 $S_{\text{qe}}(Q, \omega)$ in eq 2, expressed as

$$S_{\text{qe}}(Q, \omega) = P \int \exp\left[-\left(\frac{t}{\tau_1}\right)^{\beta_1}\right] \exp\left(i\frac{E}{\hbar}t\right) dt + (1 - P) \int \exp\left[-\left(\frac{t}{\tau_2}\right)^{\beta_2}\right] \exp\left(i\frac{E}{\hbar}t\right) dt \quad (3)$$

352 where τ and β are the characteristic time and stretching
353 exponent, respectively, while the subscripts 1 and 2 represent
354 different dynamic components. The parameter P is defined as
355 the fraction of the first Fourier-transformed stretched
356 exponential relaxation term. E is the energy change of the
357 neutrons, and \hbar is the reduced Planck constant. Using this
358 model, we expect that the rotations of methyl group can be
359 captured by the faster stretched exponential term (set $\tau_1 < \tau_2$), 360

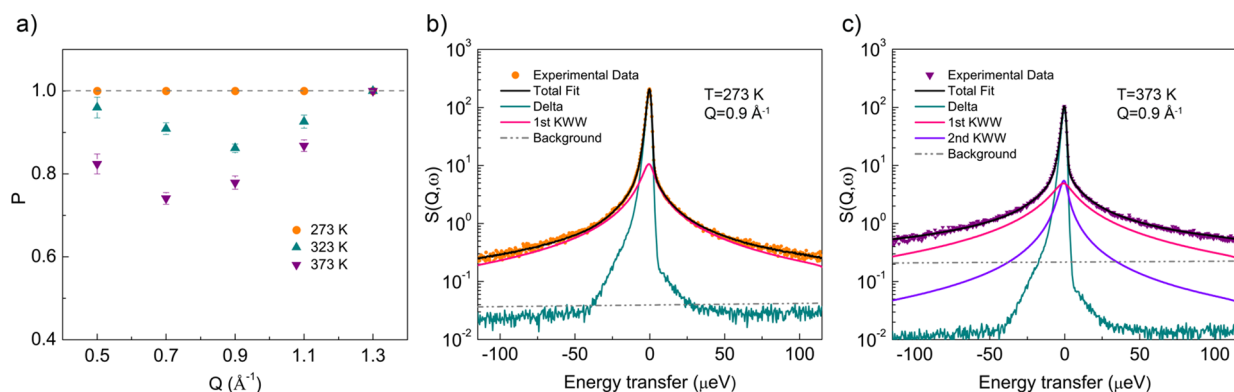


Figure 4. (a) Relative weight of the first KWW term (eq 3) as a function of Q at various temperatures. (b) Representative QENS spectrum and fit with a single KWW function of subtracted doped *d*-P3HT at a Q of 0.9 \AA^{-1} and temperature of 273 K. (c) Representative QENS spectrum and fits with two KWW functions of subtracted doped *d*-P3HT at a Q of 0.9 \AA^{-1} and temperature of 373 K.

361 while the other motion of the hydrogen sites can be captured
362 using the slower stretched exponential term.

363 We performed fits to all the spectra and found that a single
364 stretched exponential term was sufficient for satisfactory fits of
365 the 273 K data (the fit weight P values converge to unity,
366 shown in Figure 4a), but at 323 and 373 K, fitting $S_{\text{qe}}(Q, \omega)$
367 required incorporating two KWW terms for all data except $Q =$
368 1.3 \AA^{-1} . Examples of these one and two KWW fits are
369 presented in Figures 4b and 4c, respectively. As can be seen, the
370 fits capture the experimental spectra reliably over the entire
371 energy range in both cases. We attribute the successful fit using
372 only one KWW term at 273 K to the fact that the dynamics of
373 methyl group rotations dominate at a temperature that is just
374 slightly above 254 K. Reduced P values, therefore, are expected
375 once temperature increases, which is exactly what is observed.
376 The P values follow a clear decreasing trend upon heating. At
377 373 K, an average of $\sim 20\%$ of the total inelastic hydrogen
378 scattering is due to the second dynamic process. The full
379 experimental spectra and fits at all conditions are shown in
380 Supporting Information Figures S4–S6.

381 The successful fits of QENS spectra using a stretched
382 exponential model allow us to further explore the nature of the
383 dynamic motions. Normally, the mean relaxation time $\langle \tau_i \rangle$ of
384 process i is extracted by

$$\langle \tau_i \rangle = \frac{\tau_i}{\beta_i} \Gamma\left(\frac{1}{\beta_i}\right) \quad (4)$$

386 where τ_i and β_i are fitting parameters from the stretched
387 exponential model in eq 3, and $\Gamma(x)$ is the gamma function.
388 The Q^2 dependence of calculated values in the form of $\langle \tau_i \rangle^{-1}$ is
389 plotted in Figure 5. The comparison of absolute $\langle \tau_i \rangle^{-1}$ values
390 clearly implies that two distinct diffusive motions are observed
391 as expected. In addition, Figure 5 shows that for both fast and
392 slow processes the $\langle \tau_i \rangle^{-1}$ values exhibit a quadratic behavior at
393 low Q values and then a saturation trend at high Q values. This
394 nonlinear variation of $\langle \tau_i \rangle^{-1}$ as a function of Q^2 indicates
395 noncontinuous diffusion of hydrogen sites,⁵⁴ which is
396 particularly true for the case of methyl group rotations.
397 Therefore, a well-studied jump diffusion model (Singwi–
398 Sjölander model) was employed to describe both dynamic
399 processes, given by⁵⁵

$$\frac{1}{\langle \tau \rangle} = \frac{DQ^2}{1 + DQ^2\tau} \quad (5)$$

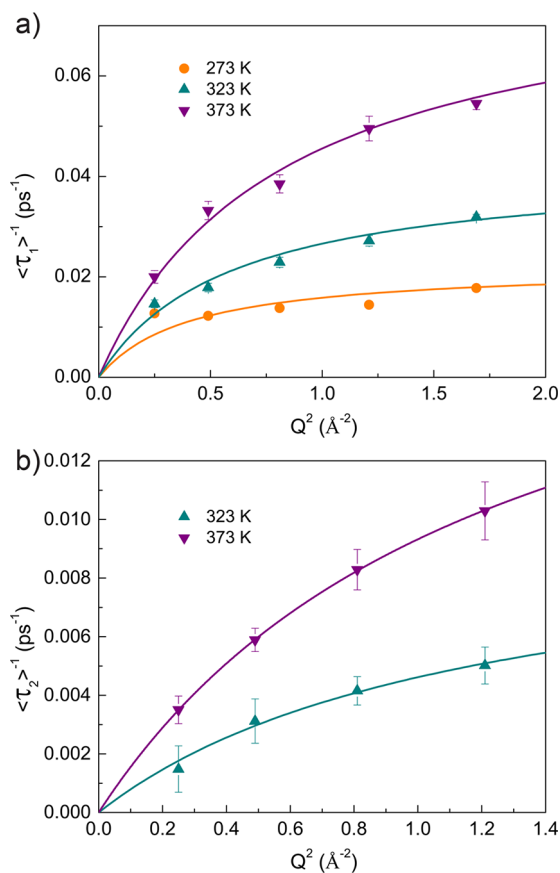


Figure 5. Inverse of mean relaxation time (symbols) of the fast process (a) and slow process (b) obtained from KWW fits as a function of Q^2 at various temperatures. The corresponding solid lines are the best representative fits to the jump diffusion model.

where τ is the residence time between jumps of a diffusive
particle and D is the diffusion coefficient. The mean-square
jump length can also be determined by $\langle L^2 \rangle = 6D\tau$ in this
model. As can be seen from the solid lines in Figure 5, these fits
yield a reasonable agreement with the data, and the resulting
diffusion parameters at each temperature are summarized in
Table 1.

By comparing the two dynamic processes, we notice that the
observed diffusion coefficients of the faster process are
approximately 1 order of magnitude greater than those of the

Table 1. Model Parameters Obtained from Fits of the Q^2 -Dependent $\langle\tau_1\rangle^{-1}$ and $\langle\tau_2\rangle^{-1}$ Using a Jump Diffusion Model

	temp (K)	diffusion coeff D ($\times 10^{-6}$ cm ² /s)	residence time τ (ps)	mean jump length $(\langle L^2 \rangle)^{1/2}$ (Å)
fast process	273	3.13 ± 1.05	34.38 ± 8.50	2.54 ± 0.74
	323	5.90 ± 0.90	20.23 ± 1.62	2.68 ± 0.31
	373	10.17 ± 0.89	12.13 ± 0.64	2.72 ± 0.19
slow process	273			
	323	0.86 ± 0.12	100.15 ± 18.01	2.27 ± 0.26
	373	1.68 ± 0.15	46.57 ± 10.22	2.17 ± 0.34

411 slower process. Also, the residence time values are factor of 5
412 lower at the same temperature for the faster process. The mean
413 jump lengths, on the other hand, are comparable at 2–3 Å.
414 With respect to the individual process, the rotational diffusion
415 coefficient of the methyl group increases from 3.13×10^{-6}
416 cm²/s at 273 K to 10.2×10^{-6} cm²/s at 373 K. Although we are
417 unable to capture the slower motion process at 273 K, the
418 diffusion coefficient of the second dynamic process still exhibits
419 a 2-fold increase from 323 to 373 K.

420 Further analysis of the temperature dependence of the
421 diffusion coefficients and residence time was performed. Here,
422 Arrhenius behavior was assumed to fit the data (seen in Figure
423 6) and an activation energy E_A associated with each process was

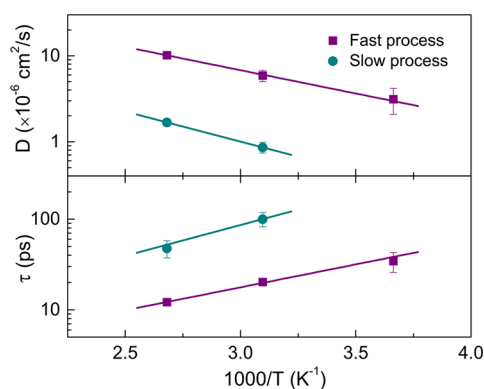


Figure 6. Diffusion coefficient (top) and residence time (bottom) as a function of $1000/T$ for the first dynamic (purple circles) and second dynamic (dark cyan squares). The corresponding solid lines are fits to an Arrhenius behavior.

424 determined, which is summarized in Table 2. As can be seen,
425 the activation energy of the slow process (~ 14 kJ/mol) is
426 slightly higher than that of the fast process (~ 10 kJ/mol).

Table 2. Activation Energy E_A (kJ/mol) Obtained from Arrhenius Fits of Diffusion Coefficient D and Residence Time τ Associated with Dynamics of Hydrogen Atoms^a

	E_A from diffusion coeff (kJ/mol)	E_A from residence time (kJ/mol)	E_A from elastic scattering (kJ/mol)
fast process	10.4 ± 0.5	9.6 ± 0.8	7.0 ± 0.3
slow process	13.4 ± 2.8	14.9 ± 4.4	

^aThe E_A value derived from elastic scattering is also shown for comparison.

Generally, the E_A of methyl group rotation is reported to be 6–12 kJ/mol for small molecules^{56–58} and polymers.^{51,59–61} To more accurately determine the E_A for this specific sample, we first performed density-functional theory (DFT) calculations on an isolated dopant molecule. The F4MCTCNQ methyl hydrogens were rotated through 120° in 30° increments with the rest of the atoms in the system fixed. As can be seen in Figure 7b (orange curve), the energy barrier to methyl rotation occurs at a 60° offset from the global minimum energy configuration. The calculated barrier of ~ 4 kJ/mol is roughly consistent with the experimental barrier of ~ 10 kJ/mol. However, since this calculated energy barrier could also be affected by the P3HT chains, the barrier in the presence of fixed chains was investigated, and the actual barrier is likely to be between these values. We assumed here, based on the published geometry of P3HT in the presence of F4TCNQ,^{62,63} that a F4MCTCNQ molecule is sandwiched between two M8 chains as seen in Figure 7a. Given the possible sensitivity to the M8 chain distance, calculations at two distinct intermolecular separations (6.30 and 6.96 Å) were performed. Figure 7b shows that the magnitude of the rotational barrier increases slightly with increasing interchain separation. In both cases, the barrier to methyl rotation was determined to be 8–10 kJ/mol, yielding a linear distance of 1.8 Å and arc length of 2.1 Å for moved hydrogen atom in this rotation. Given the typical errors of this type of calculation of at least 1 kcal/mol (~ 4 kJ/mol), this result is consistent with the QENS experiments. The value of the jump length, however, is a slightly lower than that determined experimentally, which could be due to the approximations made in the calculations, which were performed in vacuum at zero temperature and with fixed positions for the thiophene backbone. The good match between QENS experiments and DFT calculations validate the assignment of the fast dynamic process to the methyl rotation of F4MCTCNQ.

With regard to the slower observed motion, we can confidently rule out based on DFT calculations that it is due to the translational diffusion of F4MCTCNQ along the polymer backbone. Figure 7c shows the calculated energy profile for the translation of a F4MCTCNQ molecule for one thiophene unit (~ 4 Å) in each direction from its lowest energy position for the 6.96 Å separation and half a thiophene unit (~ 2 Å) in each direction for the 6.30 Å separation. The closer interchain distance between thiophene chains yields substantially higher energy barriers to translation in both directions (~ 60 kJ/mol). However, even calculation using a larger interchain separation still yields a large energy barrier of ~ 30 kJ/mol. Extending the translation for the larger interchain distance to one thiophene unit demonstrates local minima at every half-thiophene unit translation, corresponding to F4MCTCNQ ring stacking directly over a thiophene ring. In any case, the calculated translational barriers are considerably higher than what were measured experimentally from QENS (~ 14 kJ/mol).

Given the small activation energy and jump length of the slower motion, it seems more reasonable that this motion is associated with a localized motion that is internal to the F4MCTCNQ molecule. Closer inspection of the translation calculations in Figure 7c implies that low-energy vibrational motion around the position minima may be responsible for the slower motion. In other words, the whole F4MCTCNQ molecule might move back and forth within a potential well. However, further calculations using a simple harmonic

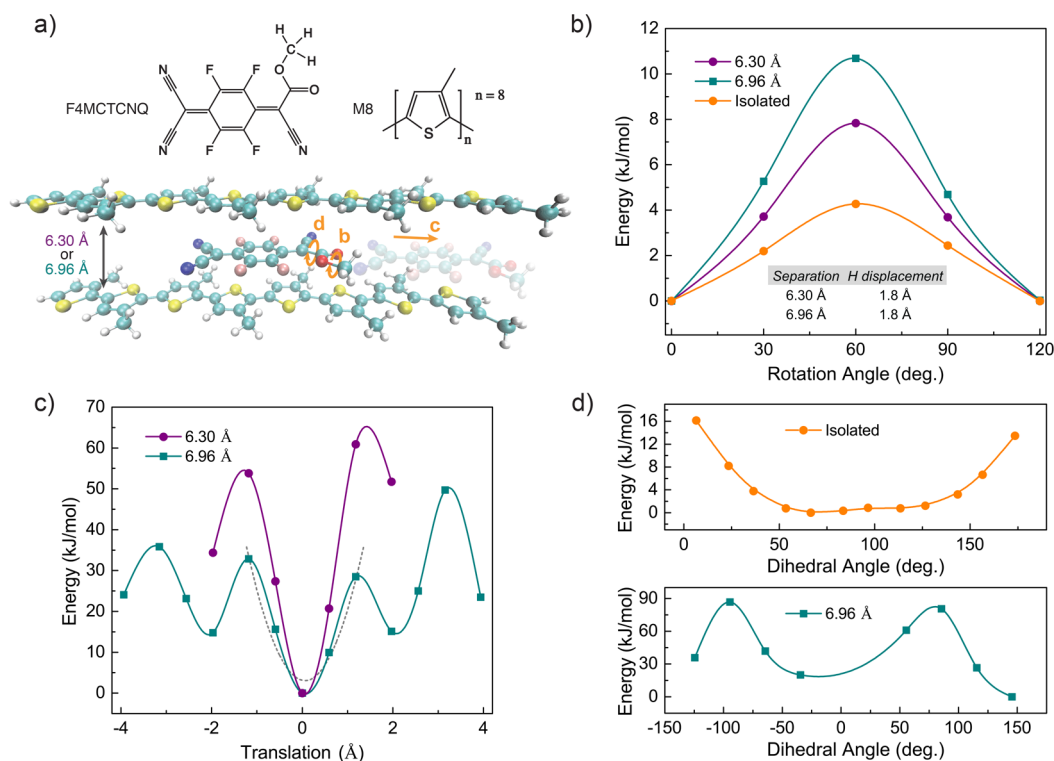


Figure 7. (a) Sandwich geometry comprising two M8 oligomers and a F4MCTCNQ molecule. The corresponding diffusive motions of each DFT calculations are also described schematically. (b) Rotation energy of the ester methyl hydrogens through 120° for two interchain separations and the isolated dopant molecule. Inset: calculated hydrogen displacements for the F4MCTCNQ methyl rotation. (c) Translation energy of the monoester molecule over one thiophene unit (6.30 Å interchain separation) and two thiophene units (6.96 Å interchain separation). The dashed gray line is the quadratic fit in order to yield a harmonic potential. (d) Rotation energy of ester group for the isolated dopant molecule (top) and a 6.96 Å interchain separation (bottom).

490 oscillator model, shown as the dashed gray line in Figure 7c,
 491 enable us to disprove this hypothesis. The calculated energy
 492 spacing between vibrational energy levels (~ 2.5 meV,
 493 Supporting Information section 6) is significantly higher than
 494 the energy spread of the QENS measurements (on the order of
 495 μeV), indicating that it is impossible to capture this dynamic
 496 motion in the energy window on BASIS. Other possible sources
 497 of the slower motion are the localized rotation of methoxy-
 498 carbonyl group ($-\text{COOCH}_3$) or the rotation of methoxy group
 499 ($-\text{OCH}_3$) in F4MCTCNQ. We can safely rule out the
 500 methoxy rotation assignment because of its high rotation
 501 barrier (>50 kJ/mol) in the literature calculations even for an
 502 isolated molecule.^{64,65} On the other hand, DFT calculations of
 503 the methoxycarbonyl rotation of an isolated F4MCTCNQ
 504 molecule (Figure 7d) yields a barrier of ~ 16 kJ/mol, which is
 505 consistent with the QENS results. Although the calculation on
 506 the sandwich geometry (6.96 Å interchain separation) produces
 507 a significantly higher barrier, a lower value would be expected if
 508 the relaxation of the chains were allowed. In addition, given the
 509 fact that the inferred E_A values of the slower motion are in good
 510 agreement with reported values for methoxycarbonyl rota-
 511 tions,⁶⁵ we tentatively assign the slower motion to this rotation
 512 of the dopant.

513 Additional insight, particularly into the geometry of the
 514 motion, can also be obtained by investigating the elastic
 515 incoherent structure factors (EISF). The Q -dependent EISF
 516 values at three investigated temperatures are plotted in Figure
 517 8. A 3-fold jump model has been widely used to describe
 518 methyl group rotations:^{66,67}

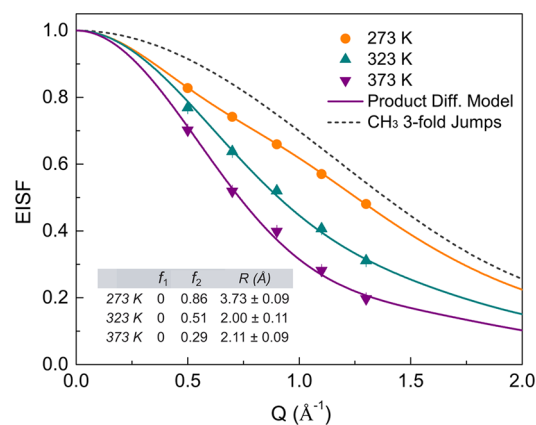


Figure 8. Elastic incoherent structure factor (EISF) obtained for subtracted doped d -P3HT as a function of Q at 273 K (orange), 323 K (dark cyan), and 373 K (purple). The solid lines are product fits to a rotational jump diffusion on a circle model (set $N = 30$ in eq 7) and a methyl group 3-fold jump model. The 3-fold jump model of the methyl group is also shown for comparison. Inset: obtained EISF fit parameters using the product diffusion model in form of eq 7.

$$\text{EISF}_{\text{methyl}}(Q) = f_1 + (1 - f_1) \left(\frac{1}{3} [1 + 2j_0(\sqrt{3}Qr)] \right) \quad (6)$$

where j_0 is the spherical zeroth-order Bessel function, f_1 is the fraction of immobile protons, and r is the radius, which was set to 1.03 Å based on the known geometry of methyl group.⁶⁸ However, the fit of methyl group 3-fold jumps (dashed line) shows significant deviation from the EISF values and is also

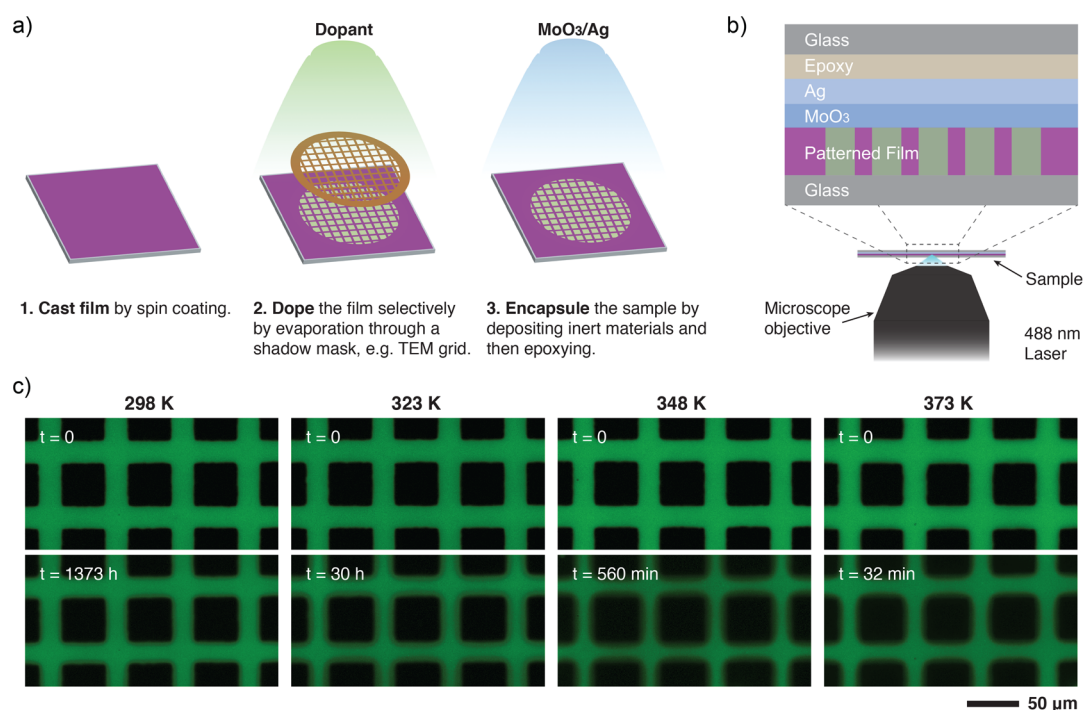


Figure 9. Schematics of (a) sample preparation and (b) resulting sample geometry and confocal experimental setup. (c) The confocal fluorescence images of patterned films before (top row) and after (bottom row) annealing at various temperatures (298, 323, 348, and 373 K) for time t .

525 greater in all cases. This clearly indicates that the methyl group
526 rotation is not the only component that contributes to the
527 QENS signal even at 273 K and that the slower motion must
528 also be taken into account, which again is in good agreement
529 with our observations from the elastic QENS data. Therefore,
530 we rewrite eq 6 by including a well-established rotational
531 diffusion model, where it is assumed that the scattering center
532 jumps between N equivalent points on a circle:^{69,70}

$$\text{EISF}(Q) = \left[f_1 + (1 - f_1) \left(\frac{1}{3} [1 + 2j_0(\sqrt{3}Qr)] \right) \right] \times \left[f_2 + (1 - f_2) \left(\frac{1}{N} \sum_{i=1}^N j_0 \left(2QR \sin \frac{\pi i}{N} \right) \right) \right] \quad (7)$$

534 where f_2 is the fraction of immobile protons involved in the
535 methoxycarbonyl rotation, R is the circle radius, and r is still set
536 to 1.03 Å. The product form means that the whole methyl
537 group moves during the methoxycarbonyl rotation. The
538 detailed derivation is shown in Supporting Information section
539 1. For $N \rightarrow \infty$, the limiting case of continuous rotational
540 diffusion on a circle is reached. By means of this improved
541 model, the EISF behavior is able to be captured over the whole
542 investigated Q range as seen the solid lines in Figure 8 where N
543 is set to 30 (a satisfactory fit is found for $N \geq 2$). In all cases,
544 the parameter f_1 always converges to 0, revealing that all
545 hydrogen sites are involved in the methyl rotations at any given
546 temperature. The parameter f_2 and R , on the other hand, are
547 found to vary slightly and converge with increasing N (Figure
548 S7), the corresponding converged values of which are
549 summarized in the inset of Figure 8. As can be seen, the
550 values of f_2 follow a clear decreasing trend from 0.86 to 0.29
551 upon heating, which is consistent with results from Figure 4
552 that increased scattering from the slower motion is observed as
553 temperature increases. Moreover, the diffusive motion of the

554 slower motion is restricted on a circle of ~ 2.0 – 3.7 Å radius, 554
555 which is also consistent with the geometry of the methoxy- 555
556 carbonyl rotation, where the distance from the center of methyl 556
557 hydrogen sites to the rotation axis is estimated to be ~ 1.7 Å. 557

Part Two: Macroscopic Dynamics of Molecular Dopants. The previous section demonstrated that two
559 molecular-scale motions of F4MCTCNQ in P3HT can be
560 observed and assigned from QENS experiments. Unfortunately,
561 the energy window of the BASIS spectrometer was insufficient
562 to observe rarer and longer-range diffusive processes that
563 contribute to macroscopic diffusion. Therefore, laser scanning
564 confocal microscopy (LSCM) was used to quantify the
565 macroscopic diffusion of F4MCTCNQ in P3HT. 566

In order to make this macroscopic measurement possible, a
567 specific sample architecture was required, which was derived
568 from our recently developed dopant-induced solubility control
569 (DISC) patterning method.¹³ Schematics of the sample
570 preparation and resulting sample geometry are shown in
571 Figures 9a and 9b, respectively, and a detailed sample
572 description is provided in the Experimental Section. It is
573 worth emphasizing that it is very important to insert a MoO₃
574 (or similarly performing oxide) layer between the patterned
575 film and the Ag layer in this experiment because the high work
576 function MoO₃ (WF = 6.8 eV) can act as an insulator to
577 prevent dopant–metal reactions.⁷¹ It is also well-known that
578 the fluorescence (FL) of P3HT is quenched by the presence of
579 dopants or any electron-accepting molecules.^{72–75} By mapping
580 out the FL intensity from LSCM and combining with a
581 calibration curve (Figure S8), we were able to track the dopant
582 concentration in the P3HT film spatially and temporally. We
583 assumed here that there was no vertical concentration gradient
584 of dopants, and thus all diffusion occurs within the two-
585 dimensional plane of the P3HT film. This assumption is valid
586 considering that the P3HT film is only 50 nm thick and
587 fluorescence is measured spatially over ~ 1 – 10 μm. Figure 9c

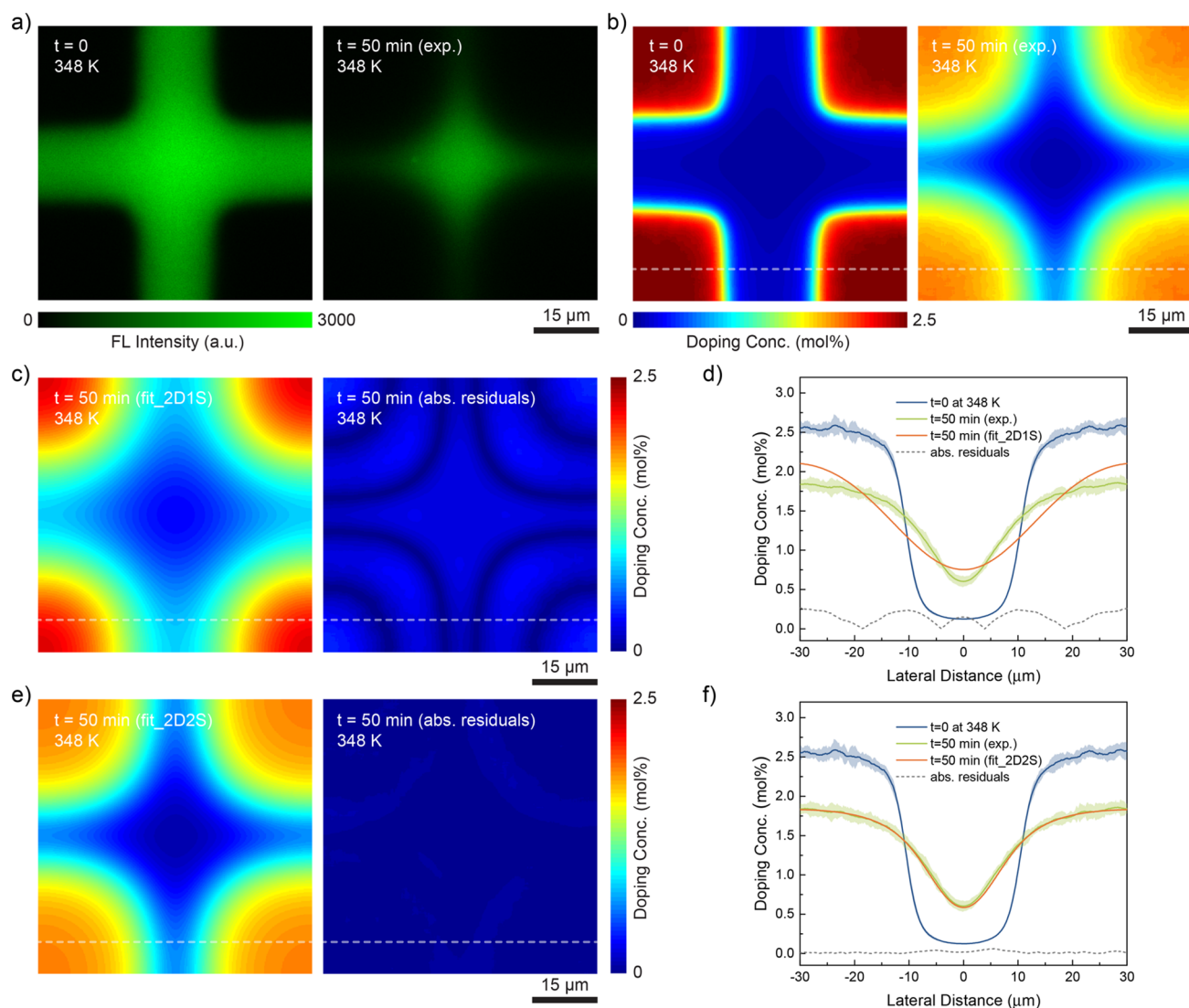


Figure 10. (a) LSCM fluorescence images of patterned F4TCNQ/P3HT films before (left) and after (right) annealing at 348 K for 50 min. (b) The 2D doping concentration maps converted from LSCM fluorescence images using a calibration curve at $t = 0$ (left) and $t = 50$ min (right). (c) The 2D doping concentration maps for a two-dimensional one-species (2D1S) model fit (left) and its absolute residuals (right). (d) Cross-sectional doping concentration profiles through images in (b) and (c) (indicated by white dashed lines) using a 2D1S diffusion model. (e) The 2D doping concentration maps for a two-dimensional two-species (2D2S) model fit (left) and its absolute residuals (right). (f) Cross-sectional doping concentration profiles through images in (b) and (e) (indicated by white dashed lines) using a 2D2S diffusion model.

589 show examples of confocal FL images before (top) and after
 590 (bottom) annealing for a time t at four different temperatures.
 591 The narrowing gaps in the FL intensity clearly indicate that the
 592 F4MCTCNQ diffuses from the doped (dark) regions to the
 593 undoped (bright) regions in the sample over time, as expected.
 594 Preliminary analysis based upon the annealing time at the
 595 different temperatures suggests that the macroscopic diffusion
 596 rate of the dopant is at least 1 order of magnitude higher for
 597 every 25 K temperature increase from 298 to 373 K.

598 We quantified the macroscopic diffusion rate and mechanism
 599 by fitting the dopant concentration as a function of lateral
 600 position and diffusion time. The F4TCNQ/P3HT system was
 601 used to validate our models. Initially, we attempted to fit the
 602 data by using a one-dimensional (1D) Fickian diffusion model
 603 that has been used previously to determine the diffusion
 604 coefficient of PCBM in a P3HT film,²⁰ the details of which are
 605 shown in Figure S9. This 1D model does not successfully
 606 capture the F4TCNQ diffusion behavior. Therefore, we

extended this 1D model to a two-dimensional, one-species
 (2D1S) diffusion model, which appeared to be more realistic.
 Images of $60 \times 60 \mu\text{m}$ were used for all the fits in order to save
 computational time. The experimental confocal FL images
 before and after annealing at 348 K for 50 min and converted to
 2D doping concentration maps are presented in Figures 10a
 and 10b, respectively, both of which clearly show F4TCNQ
 diffusion. For this 2D1S model, only one diffusive species was
 taken into account. The model fit and corresponding residuals
 are shown in Figure 10c. A direct comparison of cross-sectional
 profiles from these experimental and fitting images (indicated
 by the white dashed lines in Figures 10b and 10c, respectively)
 is also shown in Figure 10d. Again, a single diffusing species
 model yields an unsatisfactory fit for dopants concentration
 versus temperature and time, which can be seen from the
 discrepancy between measured (green line) and fit (red line)
 doping levels.

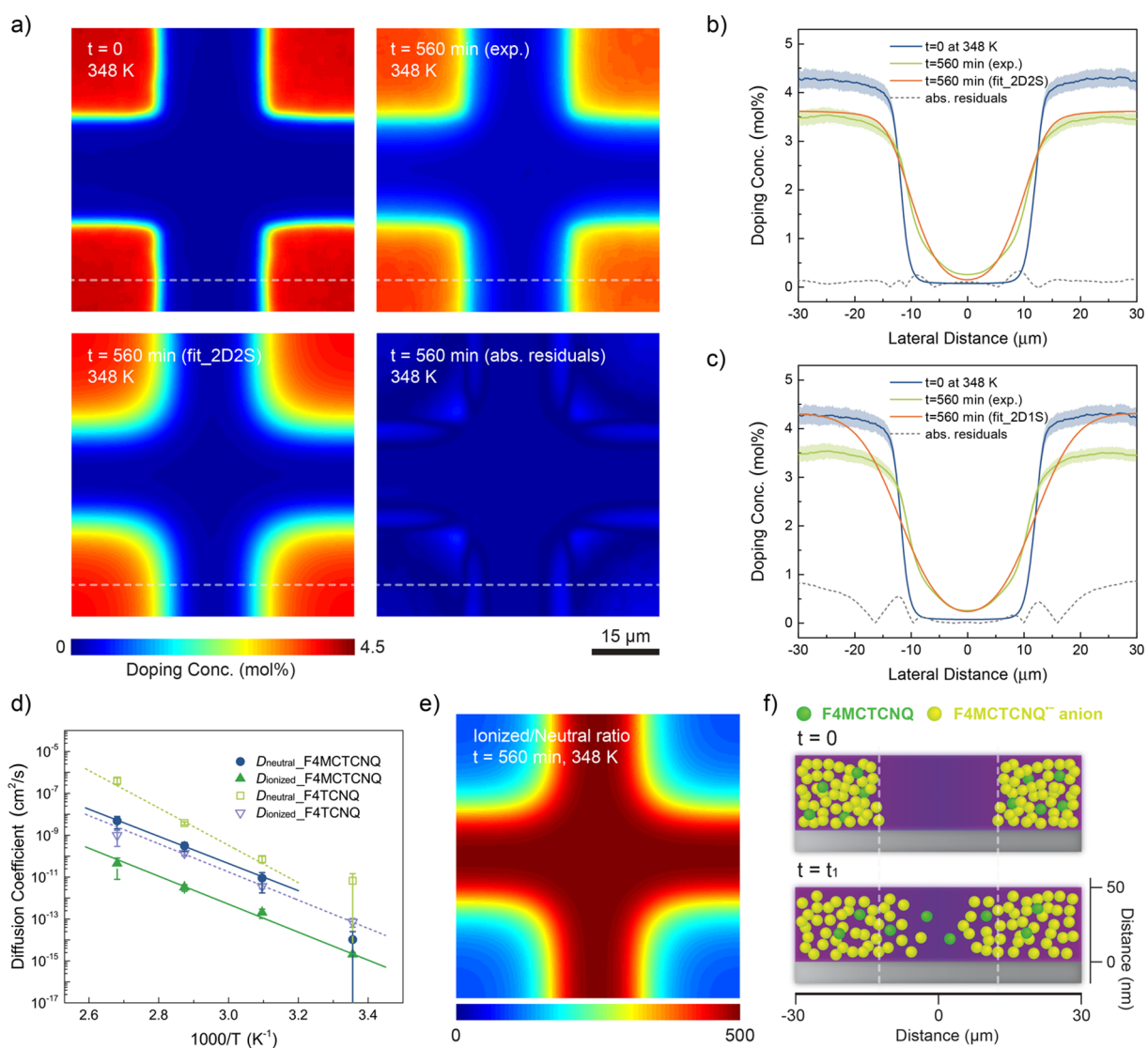


Figure 11. (a) A representative F4MCTCNQ diffusion fit at 348 K using a two-dimensional two-species (2D2S) model. 2D doping concentration maps were obtained experimentally from LSCM at $t = 0$ (top left) and $t = 560$ min (top right), 2D2S fit (bottom left), and absolute residuals (bottom right). (b) Cross-sectional doping concentration profiles through images in (a) (indicated by white dashed lines) using a 2D2S diffusion model. (c) Cross-sectional doping concentration profiles using a two-dimensional one-species (2D1S) diffusion model. (d) Determined two diffusion coefficients from 2D2S fits as a function of annealing temperatures for F4MCTCNQ (solid symbols) and F4TCNQ (open symbols) as well as corresponding Arrhenius fits. (e) 2D mole ratio profiles of slower (ionized) species to faster (neutral) species at $t = 560$ min at 348 K for F4MCTCNQ diffusion. (f) Schematic of F4MCTCNQ dopant diffusion derived from 2D2S diffusion model analysis.

624 We recently showed that an equilibrium between neutral
 625 F4TCNQ and ionized F4TCNQ exists in sequentially
 626 processed doped P3HT films, which can be described by
 627 $F4TCNQ + P3HT \rightleftharpoons F4TCNQ^- + P3HT^+$.¹⁴ In the cited
 628 study, F4TCNQ was added into the P3HT film using an
 629 orthogonal solvent. We showed that the orthogonal solvent
 630 could not dissolve or deposit F4TCNQ into the crystalline
 631 domains of P3HT, but instead only doped the amorphous
 632 domains of the polymer. In addition, we quantified the site
 633 density versus doping level for doping of the amorphous P3HT
 634 using a Langmuir isotherm model. We posit that the same
 635 model is very likely to explain the equilibrium for the F4TCNQ
 636 dopant in evaporation patterned P3HT films. The Langmuir
 637 isotherm model can be expressed as

$$\theta = \frac{C_{\text{ionized}}}{C_{\text{sat}}} = \frac{K_{\text{eq}} C_{\text{neutral}}}{1 + K_{\text{eq}} C_{\text{neutral}}} \quad (8)$$

639 where θ is the fraction of occupied doping sites in the
 640 amorphous domains of the film, C_{ionized} is the film doping
 641 concentration, C_{sat} is the saturated film doping concentration,
 642 C_{neutral} is the concentration of neutral dopant molecules, and
 643 K_{eq} is the equilibrium constant.

644 Given that both neutral and ionized dopants coexist in this
 645 sample, we developed a two-dimensional two-species (2D2S)
 646 diffusion model assuming (1) that the neutral and ionized
 647 species obey the aforementioned Langmuir isotherm equi-
 648 librium and (2) that the rate of equilibration between the two
 649 species is much faster than the rate of diffusion. Since increasing
 650 the temperature would shift the equilibrium toward a higher
 651 population of neutral dopants, the temperature-dependent K_{eq}
 652 $= \exp(-\Delta G^\circ / (k_B T))$, where ΔG° is taken to be the HOMO-
 653 LUMO difference between P3HT and the dopant (i.e., roughly
 654 the change in energy of the charge transfer process; 0.23 eV for
 655 F4TCNQ and 0.14 eV for F4MCTCNQ³⁶), k_B is the constant, 655

656 and T is the temperature. The 2D mapped doping
 657 concentration profiles were then fit with a 2D solution to
 658 Fick's second law, yielding a diffusion coefficient for each
 659 diffusive species (denoted as D_{neutral} and D_{ionized} in order to
 660 differentiate them from the diffusion coefficients obtained from
 661 QENS). The performed 2D2S fit for the F4TCNQ diffusion at
 662 348 K is shown in Figure 10e. By comparing the experimental
 663 and fit doping concentration profiles and inspecting the low
 664 residual between the data and fit in Figures 10b and 10e, it is
 665 clear that this 2D2S model is able to reproduce the lateral
 666 diffusion rates and mechanism in a consistent manner. Cross-
 667 sectional profiles through these images (indicated by the white
 668 dashed lines) are shown in Figure 10f and directly compared
 669 with the 2D2S fit. A full comparison between 2D1S and 2D2S
 670 model fits for F4TCNQ diffusion at other investigated
 671 temperatures can be found in Figures S10 and S11.

672 This 2D2S diffusion model was applied to describe the
 673 diffusion of F4MCTCNQ in the P3HT films. A representative
 674 example of the 2D2S fit for F4MCTCNQ at 348 K is shown in
 675 Figure 11a, and the cross-sectional doping concentration
 676 profiles through these images are provided in Figure 11b.
 677 The fits at other investigated temperatures can be found in
 678 Figure S12. Similar to the case of F4TCNQ, satisfactory fits can
 679 be produced. For consistency, the 2D1S model fits on
 680 F4MCTCNQ were also performed, and the resulting cross-
 681 sectional profiles at the same position are shown in Figure 11c
 682 (corresponding 2D images are presented in Figure S13). The
 683 discrepancy between measured and fit doping levels, especially
 684 in the doped region, using the 2D1S model again shows that a
 685 two species diffusion model is necessary to fit the diffusion data
 686 with sufficient accuracy. Additionally, since the highest doping
 687 ratio of ~ 4.3 mol % in the feature centers is much lower than
 688 the reported saturated doping level (>17 mol %),^{36,62} it is
 689 reasonable to assume that ionized dopants are the majority of
 690 the diffusive species in the system. Also, since the highest
 691 doping ratio is below the C_{sat} determined for the amorphous
 692 domains of P3HT in the previous study,¹⁴ it is likely that most
 693 or all of the dopants are located in and transported through the
 694 amorphous domains of P3HT.

695 The resulting two diffusion coefficients of the faster and
 696 slower species obtained from the 2D2S diffusion model are
 697 plotted as a function of the inverse of the annealing
 698 temperatures ($1000/T$) in Figure 11d. As can be seen, two
 699 distinct diffusion coefficients are observed. The diffusion
 700 coefficient of the faster species D_{neutral} is approximately 2–3
 701 orders of magnitude greater than that of the slower species
 702 D_{ionized} at the same temperature for both the F4MCTCNQ and
 703 F4TCNQ dopants in P3HT. Since the Langmuir isotherm
 704 model tracks the number of available doping sites in the P3HT,
 705 it is reasonable that the ratio of ionized to neutral dopants
 706 increases with reduced doping density. The mole ratio of the
 707 ionized (slower) to neutral (faster) dopant species is therefore
 708 tracked in this diffusion model. A representative 2D map of the
 709 ionized/neutral doping ratio for F4MCTCNQ/P3HT at 348 K
 710 is shown in Figure 11e. It is clear that the concentration of
 711 neutral species is orders of magnitude lower than the ionized
 712 species (also seen in Figure S14) and that this ratio is position-
 713 dependent, reflecting the local equilibrium between unfilled
 714 P3HT sites and dopants. Additionally, the ratio of ionized to
 715 neutral molecules increases as a function of diffusion distance,
 716 from ~ 100 in the initially doped region to ~ 500 in the initially
 717 undoped region (Figure S14). This increased ratio implies that
 718 the neutral dopant can diffuse for longer times in the highly

719 doped part of the sample, where there are fewer free undoped
 720 sites on the P3HT. As the dopant leaves the highly doped
 721 region, the neutral dopant is presented with a large number of
 722 free doping sites and so readily binds. The two-species diffusion
 723 processes is illustrated schematically in Figure 11f.

724 Since the temperature-dependent diffusion coefficients
 725 follow, within error, Arrhenius behavior (the straight lines in
 726 Figure 11d), we are able to determine the activation energy E_A
 727 associated with the diffusion process for each species. In our
 728 calculations, the D_{neutral} values at 298 K are excluded due to
 729 their uncertainties, seen from the large error bars in Figure 11d.
 730 The determined E_A values for translational diffusion are listed
 731 in Table 3. Interestingly, the E_A values for both neutral and

Table 3. Activation Energy E_A (kJ/mol) for Translational Diffusion Obtained from Arrhenius Fits of Diffusion Coefficients (D_{neutral} and D_{ionized}) of Neutral and Ionized Dopant Molecules, Respectively^a

	$E_{A_{\text{neutral}}}$ (kJ/mol)	$E_{A_{\text{ionized}}}$ (kJ/mol)
F4MCTCNQ	53.8 ± 1.9	55.5 ± 2.4
F4TCNQ	74.2 ± 7.3	55.9 ± 2.6

^a E_A values of F4TCNQ diffusions are also shown for comparison.

732 ionized F4MCTCNQ (~ 55 kJ/mol) are consistent with the
 733 translational barriers from DFT calculations in Figure 7c
 734 (especially for the smaller interchain separation). We note that
 735 the jump distance for an ionized dopant depends strongly on
 736 the energy landscape. As can be seen from Figure 7c, an open
 737 site (no other dopant in the path) and sufficient energy to
 738 surmount a 50–60 kJ/mol barrier for hopping to the next site
 739 are required for the ionized species to jump into the nearby
 740 potential well that is one bond. In addition, Kramer's theory
 741 was applied to estimate the diffusion coefficient of the dopant
 742 based on the DFT potential energy curves (Supporting
 743 Information section 11). The calculation yields a diffusion
 744 coefficient for ionized F4MCTCNQ of 1.4×10^{-14} cm²/s at
 745 298 K, which again falls into the range measured in the confocal
 746 experiments. However, the geometry of the DFT calculations
 747 depicted a highly simplified ordered P3HT domain, which is
 748 likely to different from the amorphous P3HT domain in which
 749 the dopant is expected to reside at the doping density used in
 750 the experiment. Given this discrepancy between the simulated
 751 geometry and likely sample geometry, we speculate that the
 752 measured $E_{A_{\text{ionized}}}$ likely represents an average value and that
 753 the actual hopping barriers in amorphous domains will be more
 754 heterogeneous than those estimated in the DFT calculations.

755 In addition, we can infer from the diffusion model that the
 756 jump distance for the neutral dopant is considerably larger than
 757 for the ionized dopant, even though their activation energies are
 758 similar. We know that the neutral dopant is not Coulombically
 759 bonded to the P3HT. We also know from the comparison of
 760 the 2D1S and 2D2S models that the neutral species is needed
 761 to explain the bulk diffusion profile as a function of time and
 762 temperature. It can be seen that the jump attempt frequency for
 763 the neutral and ionized molecules are similar, since since this is
 764 related to the size of the molecule and the curvature of the
 765 potential energy surface, which are likely similar of the two
 766 species. However, the jump distance is not determined from the
 767 Arrhenius fit but rather by the availability of binding sites. For
 768 an ionized dopant, the next binding site is one thiophene unit
 769 away, and thus the jump distance is smaller. For the neutral
 770 dopant, the next binding site is on average a much larger

771 distance so although the neutral species is a minority species
772 and has a similar jump attempt frequency to ionized
773 F4MCTCNQ, the macroscopic diffusion is largely driven by
774 the diffusive motion of neutral dopant molecules.

775 Finally, comparing the diffusion coefficients of F4TCNQ to
776 F4MCTCNQ, we note that F4TCNQ and F4TCNQ⁻
777 respectively diffuse approximately 10–100 times faster than
778 F4MCTCNQ and F4MCTCNQ⁻ at investigated temperatures
779 (Figure 11d). However, the $E_{A, \text{neutral}}$ of F4TCNQ is shown to
780 be higher than that of F4MCTCNQ. The reduced global
781 diffusion of F4MCTCNQ, therefore, indicates that the methyl
782 ester side chain on the F4MCTCNQ somehow reduces its
783 jump distance. To pin down the reason for the reduced
784 diffusion rate of the substituted dopant, we will present detailed
785 comparisons of temperature-dependent as well as time-
786 dependent diffusion coefficients between F4TCNQ and its
787 soluble analogues in a separate and upcoming paper. In
788 addition, examining reported diffusion studies on PCBM in the
789 P3HT matrix, we can also conclude that the diffusions of
790 molecular dopants F4TCNQ and F4MCTCNQ are faster than
791 that of PCBM in the P3HT ($D \approx 10^{-14}$ cm²/s^{76–78} and $D =$
792 $\sim 10^{-11}$ cm²/s⁷⁹ at around 413 K).

793 The results and model presented here represent the first
794 detailed mechanistic study of a specific dopant diffusing in a
795 specific semicrystalline semiconducting polymer. The results
796 and model could be applicable to a wider and more general
797 model for dopant diffusion in a wide variety of organic
798 semiconductors. For this model to be generally applicable, a
799 large number of different dopants would need to be
800 investigated in a large number of different semiconductors.
801 Also, a general means to determine the temperature-dependent
802 binding energies for dopants and the energy landscape for
803 OSCs is needed.

804 ■ CONCLUSION

805 In conclusion, we have unveiled the diffusion dynamics of the
806 p-type dopant, F4MCTCNQ, in the semiconducting polymer
807 P3HT for both microscopic and macroscopic time/distance
808 scales using two different techniques. From QENS experiments,
809 two local motions (<4 Å) are observed: methyl group rotations
810 with $D \approx 10^{-6}$ – 10^{-5} cm²/s and methoxycarbonyl group
811 rotations with smaller $D \approx 10^{-7}$ – 10^{-6} cm²/s, both of which
812 exhibit small E_A values (<15 kJ/mol) that are confirmed by
813 DFT calculations. The macroscopic dynamics, on the other
814 hand, are captured by an LSCM imaging technique. A two-
815 dimensional two-species model is developed to interpret this
816 long-range diffusion behavior, which includes a Langmuir
817 isotherm equilibrium between neutral and ionized dopant
818 molecules. As the dominant species, the ionized F4MCTCNQ
819 molecules exhibit slower diffusion than the neutral molecules
820 due to a much shorter jump distance. Both the activation
821 energy for diffusion and the jump distance of the ionized
822 species are in good agreement with the estimates from DFT
823 calculations associated with the translational motions of
824 F4MCTCNQ along the P3HT backbone (E_A of ~ 50 kJ/mol
825 and jump distance of ~ 2 Å). In contrast, the neutral species has
826 a significantly greater jump distance, which makes the neutral
827 species the dominant diffusing species at the macro scale.
828 Lastly, by comparing the diffusion coefficients between
829 F4MCTCNQ and F4TCNQ, we can also conclude that methyl
830 ester substitution in F4MCTCNQ not only increases
831 solubility/miscibility and thus doping effectiveness but also
832 helps to anchor dopants into position postdeposition due to

reduced diffusion. In theory, the two-dimensional one-/two- 833
species diffusion developed in this paper could be generalized 834
to determine the diffusion coefficient of any fluorescence 835
quenching species that can be evaporated into a polymer. 836
Studies of the dopant dynamics at both microscopic and 837
macroscopic levels are important for understanding the 838
degradation of organic devices as well as improving DISC 839
patterning methodology. 840

■ ASSOCIATED CONTENT

Supporting Information

The Supporting Information is available free of charge on the 841
ACS Publications website at DOI: 10.1021/acs.macro- 842
mol.7b00672. 843
844

Figures S1–S14 (PDF) 845
846

■ AUTHOR INFORMATION

Corresponding Author

*E-mail: amoule@ucdavis.edu (A.J.M.). 847
848

ORCID

Jun Li: 0000-0001-7850-3722 849
850

David M. Huang: 0000-0003-2048-4500 851
852

Ian E. Jacobs: 0000-0002-1535-4608 853
854

Thomas Harrelson: 0000-0002-8689-4273 855
856

Kunlun Hong: 0000-0002-2852-5111 857
858

Notes

The authors declare no competing financial interest. 859
860

■ ACKNOWLEDGMENTS

This project was carried out with funding from the U.S. 861
Department of Energy, Office of Basic Energy Sciences, 862
Division of Materials Sciences and Engineering, under Award 863
DE-SC0010419. The DFT work was undertaken with the 864
assistance of resources and services from the National 865
Computational Infrastructure (NCI), which is supported by 866
the Australian Government. Computational resources provided 867
by the University of Adelaide's Phoenix High Performance 868
Computing service are also gratefully acknowledged. Deuter- 869
ated P3HT was synthesized at the Center for Nanophase 870
Materials Sciences, a DOE Office of Science User Facility. A 871
portion of this research was performed at Spallation Neutron 872
Source, a DOE Office of Sciences facility. We thank Prof. Greg 873
Miller (UC Davis) for advice on the development of the
diffusion model.

■ REFERENCES

- (1) Taima, T.; Sakai, J.; Yamanari, T.; Saito, K. Doping Effects for 874
Organic Photovoltaic Cells Based on Small-molecular-weight Semi- 875
conductors. *Sol. Energy Mater. Sol. Cells* **2009**, *93*, 742–745. 876
877
- (2) Hains, A. W.; Liang, Z.; Woodhouse, M. A.; Gregg, B. A. 878
Molecular Semiconductors in Organic Photovoltaic Cells. *Chem. Rev.* 879
2010, *110*, 6689–6735. 880
- (3) Zhou, X.; Blochwitz, J.; Pfeiffer, M.; Nollau, A.; Fritz, T.; Leo, K. 881
Enhanced Hole Injection into Amorphous Hole-Transport Layers of 882
Organic Light-Emitting Diodes Using Controlled p-Type Doping. *Adv.* 883
Funct. Mater. **2001**, *11*, 310–314. 884
- (4) Reineke, S.; Thomschke, M.; Lüssem, B.; Leo, K. White Organic 885
Light-emitting Diodes: Status and Perspective. *Rev. Mod. Phys.* **2013**, 886
85, 1245–1293. 887
- (5) Braga, D.; Horowitz, G. High-Performance Organic Field-Effect 888
Transistors. *Adv. Mater.* **2009**, *21*, 1473–1486. 889
- (6) Lu, G.; Blakesley, J.; Himmelberger, S.; Pingel, P.; Frisch, J.; 890
Lieberwirth, I.; Salzmann, I.; Oehzelt, M.; Di Pietro, R.; Salleo, A.; 891

- 892 Koch, N.; Neher, D. Moderate Doping Leads to High Performance of
893 Semiconductor/insulator Polymer Blend Transistors. *Nat. Commun.*
894 **2013**, *4*, 1588.
- 895 (7) Heeger, A. J. Semiconducting and Metallic Polymers: The Fourth
896 Generation of Polymeric Materials (Nobel Lecture). *Angew. Chem., Int.*
897 *Ed.* **2001**, *40*, 2591–2611.
- 898 (8) Lüssem, B.; Riede, M.; Leo, K. Doping of Organic Semi-
899 conductors. *Phys. Status Solidi A* **2013**, *210*, 9–43.
- 900 (9) Zhao, X.; Zhan, X. Electron Transporting Semiconducting
901 Polymers in Organic Electronics. *Chem. Soc. Rev.* **2011**, *40*, 3728–
902 3743.
- 903 (10) Walzer, K.; Maennig, B.; Pfeiffer, M.; Leo, K. Highly Efficient
904 Organic Devices Based on Electrically Doped Transport Layers. *Chem.*
905 *Rev.* **2007**, *107*, 1233–1271.
- 906 (11) Olthof, S.; Tress, W.; Meerheim, R.; Lüssem, B.; Leo, K.
907 Photoelectron Spectroscopy Study of Systematically Varied Doping
908 Concentrations in An Organic Semiconductor Layer Using A
909 Molecular P-Dopant. *J. Appl. Phys.* **2009**, *106*, 103711.
- 910 (12) Lee, J. H.; Lee, J.; Kim, Y. H.; Yun, C.; Lüssem, B.; Leo, K.
911 Effect of Trap States on the Electrical Doping of Organic
912 Semiconductors. *Org. Electron.* **2014**, *15*, 16–21.
- 913 (13) Jacobs, I. E.; Li, J.; Burg, S. L.; Bilsky, D. J.; Rotondo, B. T.;
914 Augustine, M. P.; Stroeve, P.; Moulé, A. J. Reversible Optical Control
915 of Conjugated Polymer Solubility with Sub-micrometer Resolution.
916 *ACS Nano* **2015**, *9*, 1905–1912.
- 917 (14) Jacobs, I. E.; Aasen, E. W.; Oliveira, J. L.; Fonseca, T. N.;
918 Roehling, J. D.; Li, J.; Zhang, G.; Augustine, M. P.; Mascall, M.; Moule,
919 A. J. Comparison of Solution-mixed and Sequentially Processed
920 P3HT:F4TCNQ Films: Effect of Doping-induced Aggregation on
921 Film Morphology. *J. Mater. Chem. C* **2016**, *4*, 3454–3466.
- 922 (15) Jacobs, I. E.; Wang, F.; Hafezi, N.; Medina-Plaza, C.; Harrelson,
923 T. F.; Li, J.; Augustine, M. P.; Mascall, M.; Moulé, A. J. Quantitative
924 Dedoping of Conductive Polymers. *Chem. Mater.* **2017**, *29*, 832–841.
- 925 (16) Jacobs, I. E.; Aasen, E. W.; Nowak, D.; Li, J.; Morrison, W.;
926 Roehling, J. D.; Augustine, M. P.; Moulé, A. J. Direct-Write Optical
927 Patterning of P3HT Films Beyond the Diffraction Limit. *Adv. Mater.*
928 **2017**, *29*, 1603221.
- 929 (17) Tyagi, P.; Dalai, M. K.; Suman, C. K.; Tuli, S.; Srivastava, R.
930 Study of 2,3,5,6-tetrafluoro-7,7[prime or minute],8,8[prime or
931 minute]- tetracyano quinodimethane Diffusion in Organic Light
932 Emitting Diodes Using Secondary Ion Mass Spectroscopy. *RSC Adv.*
933 **2013**, *3*, 24553–24559.
- 934 (18) Dai, A.; Wan, A.; Magee, C.; Zhang, Y.; Barlow, S.; Marder, S.
935 R.; Kahn, A. Investigation of P-dopant Diffusion in Polymer Films and
936 Bulk Heterojunctions: Stable Spatially-confined Doping for All-
937 solution Processed Solar Cells. *Org. Electron.* **2015**, *23*, 151–157.
- 938 (19) Treat, N. D.; Brady, M. A.; Smith, G.; Toney, M. F.; Kramer, E.
939 J.; Hawker, C. J.; Chabynyc, M. L. Interdiffusion of PCBM and P3HT
940 Reveals Miscibility in a Photovoltaically Active Blend. *Adv. Energy*
941 *Mater.* **2011**, *1*, 82–89.
- 942 (20) Treat, N. D.; Mates, T. E.; Hawker, C. J.; Kramer, E. J.;
943 Chabynyc, M. L. Temperature Dependence of the Diffusion
944 Coefficient of PCBM in Poly(3-hexylthiophene). *Macromolecules*
945 **2013**, *46*, 1002–1007.
- 946 (21) Qi, Y.; Sajoto, T.; Kröger, M.; Kandabarow, A. M.; Park, W.;
947 Barlow, S.; Kim, E.-G.; Wielunski, L.; Feldman, L. C.; Bartynski, R. A.;
948 Brédas, J.-L.; Marder, S. R.; Kahn, A. A Molybdenum Dithiolene
949 Complex as p-Dopant for Hole-Transport Materials: A Multitechnique
950 Experimental and Theoretical Investigation. *Chem. Mater.* **2010**, *22*,
951 524–531.
- 952 (22) Li, J.; Rochester, C. W.; Jacobs, I. E.; Friedrich, S.; Stroeve, P.;
953 Riede, M.; Moulé, A. J. Measurement of Small Molecular Dopant
954 F4TCNQ and C60F36 Diffusion in Organic Bilayer Architectures.
955 *ACS Appl. Mater. Interfaces* **2015**, *7*, 28420–28428.
- 956 (23) Li, J.; Rochester, C. W.; Jacobs, I. E.; Aasen, E. W.; Friedrich, S.;
957 Stroeve, P.; Moulé, A. J. The Effect of Thermal Annealing on Dopant
958 Site Choice in Conjugated Polymers. *Org. Electron.* **2016**, *33*, 23–31.
- 959 (24) Fischer, F.; Hahn, T.; Bässler, H.; Bauer, I.; Strohriegel, P.;
960 Köhler, A. Measuring Reduced C60 Diffusion in Crosslinked Polymer
Films by Optical Spectroscopy. *Adv. Funct. Mater.* **2014**, *24*, 6172–
6177.
- (25) Tyagi, P.; Tuli, S.; Srivastava, R. Study of Fluorescence
Quenching due to 2, 3, 5, 6-Tetrafluoro-7, 7', 8, 8'-Tetracyano
Quinodimethane and Its Solid State Diffusion Analysis using
Photoluminescence Spectroscopy. *J. Chem. Phys.* **2015**, *142*, 054707.
- (26) Zhang, L.; Zu, F.-S.; Deng, Y.-L.; Igbari, F.; Wang, Z.-K.; Liao,
L.-S. Origin of Enhanced Hole Injection in Organic Light-Emitting
Diodes with an Electron-Acceptor Doping Layer: p-Type Doping or
Interfacial Diffusion? *ACS Appl. Mater. Interfaces* **2015**, *7*, 11965–
11971.
- (27) Jung, M.-C.; Qi, Y. Dopant Interdiffusion Effects in n-i-p
Structured Spiro-OMeTAD Hole Transport Layer of Organometal
Halide Perovskite Solar Cells. *Org. Electron.* **2016**, *31*, 71–76.
- (28) Gao, W.; Kahn, A. Controlled P Doping of the Hole-transport
Molecular Material N,N-diphenyl-N,N-bis(1-naphthyl)-1,1-biphenyl-
4,4-diamine with Tetrafluorotetracyanoquinodimethane. *J. Appl. Phys.*
2003, *94*, 359–366.
- (29) Kolesov, V. A.; Fuentes-Hernandez, C.; Chou, W.-F.; Aizawa,
N.; Larrain, F. A.; Wang, M.; Perrotta, A.; Choi, S.; Graham, S.; Bazan,
G. C.; Nguyen, T.-Q.; Marder, S. R.; Kippelen, B. Solution-based
Electrical Doping of Semiconducting Polymer Films over a Limited
Depth. *Nat. Mater.* **2016**, advance online publication.
- (30) Gao, Z. Q.; Mi, B. X.; Xu, G. Z.; Wan, Y. Q.; Gong, M. L.;
Cheah, K. W.; Chen, C. H. An Organic P-type Dopant with High
Thermal Stability for an Organic Semiconductor. *Chem. Commun.*
2008, 117–119.
- (31) Gao, W.; Kahn, A. Controlled P-doping of Zinc Phthalocyanine
by Coevaporation with Tetrafluorotetracyanoquinodimethane: A
Direct and Inverse Photoemission Study. *Appl. Phys. Lett.* **2001**, *79*,
4040–4042.
- (32) Dai, A.; Zhou, Y.; Shu, A. L.; Mohapatra, S. K.; Wang, H.;
Fuentes-Hernandez, C.; Zhang, Y.; Barlow, S.; Loo, Y.-L.; Marder, S.
R.; Kippelen, B.; Kahn, A. Enhanced Charge-carrier Injection and
Collection via Lamination of Doped Polymer Layers p-Doped with a
Solution-Processible Molybdenum Complex. *Adv. Funct. Mater.* **2014**,
24, 2197–2204.
- (33) Drechsel, J.; Männig, B.; Kozłowski, F.; Pfeiffer, M.; Leo, K.;
Hoppe, H. Efficient Organic Solar Cells Based on a Double p-i-n
Architecture Using Doped Wide-gap Transport Layers. *Appl. Phys.*
Lett. **2005**, *86*, 244102.
- (34) Meerheim, R.; Olthof, S.; Hermenau, M.; Scholz, S.; Petrich, A.;
Tessler, N.; Solomeshch, O.; Lüssem, B.; Riede, M.; Leo, K.
Investigation of C60F36 as Low-volatility P-dopant in Organic
Optoelectronic Devices. *J. Appl. Phys.* **2011**, *109*, 103102.
- (35) Lin, X.; Purdum, G. E.; Zhang, Y.; Barlow, S.; Marder, S. R.;
Loo, Y.-L.; Kahn, A. Impact of a Low Concentration of Dopants on
the Distribution of Gap States in a Molecular Semiconductor. *Chem.*
Mater. **2016**, *28*, 2677–2684.
- (36) Li, J.; Zhang, G.; Holm, D. M.; Jacobs, I. E.; Yin, B.; Stroeve, P.;
Mascall, M.; Moulé, A. J. Introducing Solubility Control for Improved
Organic P-type Dopants. *Chem. Mater.* **2015**, *27*, 5765–5774.
- (37) Sakai, V. G.; Arbe, A. Quasielastic Neutron Scattering in Soft
Matter. *Curr. Opin. Colloid Interface Sci.* **2009**, *14*, 381–390.
- (38) Shao, M.; Keum, J.; Chen, J.; He, Y.; Chen, W.; Browning, J. F.;
Jakowski, J.; Sumpter, B. G.; Ivanov, I. N.; Ma, Y.-Z.; Rouleau, C. M.;
Smith, S. C.; Geoghegan, D. B.; Hong, K.; Xiao, K. The Isotopic Effects
of Deuteration on Optoelectronic Properties of Conducting Polymers.
Nat. Commun. **2014**, *5*, 3180.
- (39) Mamontov, E.; Herwig, K. W. A Time-of-flight Backscattering
Spectrometer at the Spallation Neutron Source, BASIS. *Rev. Sci.*
Instrum. **2011**, *82*, 085109.
- (40) Azuah, R. T.; Kneller, L. R.; Qiu, Y.; Tregenna-Piggott, P. L.;
Brown, C. M.; Copley, J. R.; Dimeo, R. M. DAVE: A Comprehensive
Software Suite for the Reduction Visualization, and Analysis of Low
Energy Neutron Spectroscopic Data. *J. Res. Natl. Inst. Stand. Technol.*
2009, *114*, 341.
- (41) Hempelmann, R. *Quasielastic Neutron Scattering and Solid State
Diffusion*; Clarendon Press: 2000.

- (42) Langmuir, I. The Adsorption of Gases on Plane Surfaces of Glass, Mica and Platinum. *J. Am. Chem. Soc.* **1918**, *40*, 1361–1403.
- (43) Becke, A. D. Density-functional Thermochemistry. III. The Role of Exact Exchange. *J. Chem. Phys.* **1993**, *98*, 5648–5652.
- (44) Grimme, S. Semiempirical GGA-type Density Functional Constructed with a Long-range Dispersion Correction. *J. Comput. Chem.* **2006**, *27*, 1787–1799.
- (45) Ackling, S. Interplay of Structural, Dynamical, and Electronic Properties in Doped Semiconducting Polymer Systems. M.Sc. Thesis, The University of Adelaide, 2017.
- (46) Lemaur, V.; Steel, M.; Beljonne, D.; Brédas, J.-L.; Cornil, J. Photoinduced Charge Generation and Recombination Dynamics in Model Donor/Acceptor Pairs for Organic Solar Cell Applications: A Full Quantum-Chemical Treatment. *J. Am. Chem. Soc.* **2005**, *127*, 6077–6086.
- (47) Mityashin, A.; Olivier, Y.; Van Regemorter, T.; Rolin, C.; Verlaak, S.; Martinelli, N. G.; Beljonne, D.; Cornil, J.; Genoe, J.; Heremans, P. Unraveling the Mechanism of Molecular Doping in Organic Semiconductors. *Adv. Mater.* **2012**, *24*, 1535–1539.
- (48) Gregg, B. A.; Hanna, M. C. Comparing Organic to Inorganic Photovoltaic Cells: Theory, Experiment, and Simulation. *J. Appl. Phys.* **2003**, *93*, 3605–3614.
- (49) Madigan, C. F.; Bulović, V. Solid State Solvation in Amorphous Organic Thin Films. *Phys. Rev. Lett.* **2003**, *91*, 247403.
- (50) Mamontov, E.; Luo, H.; Dai, S. Proton Dynamics in N,N,N,N-Tetramethylguanidinium Bis(perfluoroethylsulfonyl)imide Protic Ionic Liquid Probed by Quasielastic Neutron Scattering. *J. Phys. Chem. B* **2009**, *113*, 159–169.
- (51) Frick, B.; Fetters, L. J. Methyl Group Dynamics in Glassy Polyisoprene: A Neutron Backscattering Investigation. *Macromolecules* **1994**, *27*, 974–980.
- (52) Ngai, K. L.; Capaccioli, S.; Paciaroni, A. Change of Caged Dynamics at T_g in Hydrated Proteins: Trend of Mean Squared Displacements after Correcting for the Methyl-group Rotation Contribution. *J. Chem. Phys.* **2013**, *138*, 235102.
- (53) Paternó, G.; Cacialli, F.; García-Sakai, V. Structural and Dynamical Characterization of P3HT/PCBM Blends. *Chem. Phys.* **2013**, *427*, 142–146.
- (54) Gautam, S.; Liu, T.; Rother, G.; Jalarvo, N.; Mamontov, E.; Welch, S.; Sheets, J.; Droege, M.; Cole, D. R. Dynamics of Propane in Nanoporous Silica Aerogel: A Quasielastic Neutron Scattering Study. *J. Phys. Chem. C* **2015**, *119*, 18188–18195.
- (55) Singwi, K. S.; Sjölander, A. Diffusive Motions in Water and Cold Neutron Scattering. *Phys. Rev.* **1960**, *119*, 863–871.
- (56) Batchelder, L. S.; Niu, C. H.; Torchia, D. A. Methyl Reorientation in Polycrystalline Amino Acids and Peptides: A Deuteron NMR Spin-lattice Relaxation Study. *J. Am. Chem. Soc.* **1983**, *105*, 2228–2231.
- (57) Takegoshi, K.; Imashiro, F.; Terao, T.; Saika, A. 1H and 13C NMR Study on Rotation of Congested Methyl Groups in Methyl Substituted Phenanthrenes, Fluorenes, and Fluorenones. *J. Chem. Phys.* **1984**, *80*, 1089–1094.
- (58) Beckmann, P. A.; Cheung, A. M.; Fisch, E. E.; Fusco, F. A.; Herzog, R. E.; Narasimhan, M. Methyl and Tertbutyl Reorientation and Distributions of Activation Energies in Molecular Solids. A Nuclear Spinrelaxation Study in 2,4 and 2,5-ditertbutylhydroxybenzene. *J. Chem. Phys.* **1986**, *84*, 1959–1968.
- (59) Chahid, A.; Alegria, A.; Colmenero, J. Methyl Group Dynamics in Poly(vinyl methyl ether). A Rotation Rate Distribution Model. *Macromolecules* **1994**, *27*, 3282–3288.
- (60) Mukhopadhyay, R.; Alegria, A.; Colmenero, J.; Frick, B. Methyl Group Dynamics in Poly(vinyl acetate): A Neutron Scattering Study. *Macromolecules* **1998**, *31*, 3985–3993.
- (61) Moreno, A. J.; Alegria, A.; Colmenero, J.; Frick, B. Methyl Group Dynamics in Poly(methyl methacrylate): From Quantum Tunneling to Classical Hopping. *Macromolecules* **2001**, *34*, 4886–4896.
- (62) Duong, D. T.; Wang, C.; Antono, E.; Toney, M. F.; Salleo, A. The Chemical and Structural Origin of Efficient P-type Doping in P3HT. *Org. Electron.* **2013**, *14*, 1330–1336.
- (63) Harrelson, T. F.; Cheng, Y. Q.; Li, J.; Jacobs, I. E.; Ramirez-Cuesta, A. J.; Faller, R.; Moulé, A. J. Identifying Atomic Scale Structure in Undoped/Doped Semicrystalline P3HT Using Inelastic Neutron Scattering. *Macromolecules* **2017**, *50*, 2424–2435.
- (64) Wiberg, K. B.; Laidig, K. E. Barriers to Rotation Adjacent to Double Bonds. 3. The Carbon-oxygen Barrier in Formic Acid, Methyl Formate, Acetic Acid, and Methyl Acetate. The Origin of Ester and Amide Resonance. *J. Am. Chem. Soc.* **1987**, *109*, 5935–5943.
- (65) Heijboer, J.; Baas, J.; van de Graaf, B.; Hoefnagel, M. A Molecular Mechanics Study on Rotational Motions of Side Groups in Poly(methyl methacrylate). *Polymer* **1987**, *28*, 509–513.
- (66) Gabrys, B.; Higgins, J. S.; Ma, K. T.; Roots, J. E. Rotational Motion of the Ester Methyl Group in Stereoregular Poly(methyl methacrylate): A Neutron Scattering Study. *Macromolecules* **1984**, *17*, 560–566.
- (67) Arrighi, V.; Higgins, J. S.; Burgess, A. N.; Howells, W. S. Rotation of Methyl Side Groups in Polymers: A Fourier Transform Approach to Quasielastic Neutron Scattering. 1. Homopolymers. *Macromolecules* **1995**, *28*, 2745–2753.
- (68) Kimura, K.; Kubo, M. Structures of Dimethyl Ether and Methyl Alcohol. *J. Chem. Phys.* **1959**, *30*, 151–158.
- (69) Barnes, J. D. Inelastic Neutron Scattering Study of the Rotator Phase Transition in N-nonadecane. *J. Chem. Phys.* **1973**, *58*, 5193–5201.
- (70) Fujara, F.; Wefing, S.; Spiess, H. W. Dynamics of Molecular Reorientations: Analogies between Quasielastic Neutron Scattering and Deuteron NMR Spin Alignment. *J. Chem. Phys.* **1986**, *84*, 4579–4584.
- (71) Winkler, S.; Amsalem, P.; Frisch, J.; Oehzelt, M.; Heimel, G.; Koch, N. Probing the Energy Levels in Hole-doped Molecular Semiconductors. *Mater. Horiz.* **2015**, *2*, 427–433.
- (72) Yim, K. H.; Whiting, G. L.; Murphy, C. E.; Halls, J. J. M.; Burroughes, J. H.; Friend, R. H.; Kim, J.-S. Controlling Electrical Properties of Conjugated Polymers via a Solution-Based p-Type Doping. *Adv. Mater.* **2008**, *20*, 3319–3324.
- (73) Tsoi, W. C.; Spencer, S. J.; Yang, L.; Ballantyne, A. M.; Nicholson, P. G.; Turnbull, A.; Shard, A. G.; Murphy, C. E.; Bradley, D. D. C.; Nelson, J.; Kim, J.-S. Effect of Crystallization on the Electronic Energy Levels and Thin Film Morphology of P3HT:PCBM Blends. *Macromolecules* **2011**, *44*, 2944–2952.
- (74) Yu, G.; Gao, J.; Hummelen, J. C.; Wudl, F.; Heeger, A. J. Polymer Photovoltaic Cells: Enhanced Efficiencies via a Network of Internal Donor-Acceptor Heterojunctions. *Science* **1995**, *270*, 1789–1791.
- (75) Ferguson, A. J.; Kopidakis, N.; Shaheen, S. E.; Rumbles, G. Quenching of Excitons by Holes in Poly(3-hexylthiophene) Films. *J. Phys. Chem. C* **2008**, *112*, 9865–9871.
- (76) Watts, B.; Belcher, W. J.; Thomsen, L.; Ade, H.; Dastoor, P. C. A Quantitative Study of PCBM Diffusion during Annealing of P3HT:PCBM Blend Films. *Macromolecules* **2009**, *42*, 8392–8397.
- (77) Labram, J. G.; Kirkpatrick, J.; Bradley, D. D. C.; Anthopoulos, T. D. Measurement of the Diffusivity of Fullerenes in Polymers Using Bilayer Organic Field Effect Transistors. *Phys. Rev. B: Condens. Matter Phys.* **2011**, *84*, 075344.
- (78) Labram, J. G.; Kirkpatrick, J.; Bradley, D. D. C.; Anthopoulos, T. D. Impact of Fullerene Molecular Weight on P3HT:PCBM Microstructure Studied Using Organic Thin-Film Transistors. *Adv. Energy Mater.* **2011**, *1*, 1176–1183.
- (79) Berriman, G. A.; Holdsworth, J. L.; Zhou, X.; Belcher, W. J.; Dastoor, P. C. Molecular versus Crystallite PCBM Diffusion in P3HT:PCBM Blends. *AIP Adv.* **2015**, *5*, 097220.